

# Journal of Materials Chemistry A

Accepted Manuscript



This is an *Accepted Manuscript*, which has been through the Royal Society of Chemistry peer review process and has been accepted for publication.

*Accepted Manuscripts* are published online shortly after acceptance, before technical editing, formatting and proof reading. Using this free service, authors can make their results available to the community, in citable form, before we publish the edited article. We will replace this *Accepted Manuscript* with the edited and formatted *Advance Article* as soon as it is available.

You can find more information about *Accepted Manuscripts* in the [Information for Authors](#).

Please note that technical editing may introduce minor changes to the text and/or graphics, which may alter content. The journal's standard [Terms & Conditions](#) and the [Ethical guidelines](#) still apply. In no event shall the Royal Society of Chemistry be held responsible for any errors or omissions in this *Accepted Manuscript* or any consequences arising from the use of any information it contains.

Cite this: DOI: 10.1039/c0xx00000x

[www.rsc.org/xxxxxx](http://www.rsc.org/xxxxxx)

ARTICLE TYPE

# Top-down Synthesis of Muscle-inspired alluaudite $\text{Na}_{2+2x}\text{Fe}_{2-x}(\text{SO}_4)_3$ /SWNT Spindle as a High-rate and High-potential Cathode for Sodium-Ion Batteries

Yu Meng<sup>a,†</sup>, Tiantian Yu<sup>b,†</sup>, Sen Zhang<sup>\*a</sup>, Chao Deng<sup>\*b</sup>

Received (in XXX, XXX) Xth XXXXXXXXX 20XX, Accepted Xth XXXXXXXXX 20XX

DOI: 10.1039/b000000x

Tailoring materials into bio-inspired structures are triggering unprecedented innovations in releasing their functional properties. Muscle tissue is composed of myofibrils and densely-wired blood vessels; it is a perfect model for designing high-performance electrode materials that have the advantage of fast mass-transport and superior durability. We design a top-down strategy as a facile approach in order to tailor the alluaudite  $\text{Na}_{2+2x}\text{Fe}_{2-x}(\text{SO}_4)_3$  into muscle-like spindle. A precipitation process is employed to prepare the hydrated “top” precursor which is subjected to dehydration and phase-transformation to obtain the “down” product. The alluaudite sulfate nanoparticles closely anchor on the single-wall carbon nanotubes, and they together aggregate into microscale particles in the shape of spindles. The  $\text{Na}_{2+2x}\text{Fe}_{2-x}(\text{SO}_4)_3$ /SWNT composite as a whole copies the morphology and function of the muscle tissue. Taking advantage of its 3D conductive framework and porous structure, the composite achieves fast electron/ion transport and sodium intercalation. Moreover, the single-phase reaction mechanism during sodium intercalation is beneficial to its cycling property. It exhibits such desirable electrochemical performance as an operating potential as high as  $\sim 3.8$  V and a high-rate capability, which achieves a capacity-retention of 92% after 100 cycles at 5 C. The muscle-inspired architecture makes electrode materials favorable for superior electrochemical performance.

KEYWORDS: Top-down synthesis; alluaudite sulfate; muscle-inspired; sodium ion battery; high-rate capability

## 1 Introduction

High-performance electrode materials are critical for fast development of energy storage systems. Over the past decades, lithium ion battery with the highest energy density is a mature technology for energy storage. However, the growing concern over the cost and availability of lithium resource has encouraged the usage of batteries based on alternate carrier ions.<sup>1,2</sup> The low cost and abundant resource of sodium make sodium-ion battery a promising alternative to lithium ion battery. Since 1980s, many materials including layered oxides (e.g.  $\text{Na}_x\text{CoO}_2$ ,  $\text{Na}_x\text{FeO}_2$ ,  $\text{Na}_x\text{MnO}_2$ ,  $\text{Na}_2\text{V}_6\text{O}_{16}\cdot n\text{H}_2\text{O}$  and  $\text{NaNi}_{1/3}\text{Mn}_{1/3}\text{Co}_{1/3}\text{O}_2$ ),<sup>3-7</sup> polyanions (e.g.  $\text{Na}_3\text{V}_2(\text{PO}_4)_3$ ,  $\text{NaTi}_2(\text{PO}_4)_3$ ,  $\text{Na}_2\text{FeP}_2\text{O}_7$ ,  $\text{NaVOPO}_4$ ,  $\text{Na}_{4-a}\text{Fe}_{2+a/2}(\text{P}_2\text{O}_7)_2$  and  $\text{Na}_2\text{FePO}_4\text{F}$ ),<sup>8-12</sup> and mixed-polyanions (e.g.  $\text{Na}_7\text{V}_3(\text{P}_2\text{O}_7)_4(\text{PO}_4)$ ,  $\text{Na}_4\text{Fe}_3(\text{PO}_4)_2(\text{P}_2\text{O}_7)$  and  $\text{Na}_3\text{FeCO}_3\text{PO}_4$ ), *et al.*<sup>13-18</sup> have been extensively investigated as sodium hosts. However, the low operating potential inhibits their application in sodium-ion batteries.

Aiming at finding high-voltage cathodes for Na-ion battery, the new sulfate family comes into sight as a promising candidate. Based on the induced effect, the stronger electronegativity and more ionic M-O band make sulfate achieve higher operating potential than other polyanion materials. A series of sulfate-based

sodium hosts, such as  $\text{Na}_2\text{M}(\text{SO}_4)_2\cdot n\text{H}_2\text{O}$  (M=Fe, Co; n=2, 4),<sup>19-21</sup>  $\text{NaFeSO}_4\text{F}$ <sup>22,23</sup> and  $\text{Na}_{2+2x}\text{M}_{2-x}(\text{SO}_4)_3$  (M=Fe, Mn),<sup>24-29</sup> has been demonstrated to have favorable sodium intercalation capability. The exploration of these sulfate-based compounds dramatically expands the research scope of sodium intercalation chemistry and provides new alternative for high-voltage electrode materials in sodium ion batteries.

Among the present sulfate materials, a recently reported iron-based sulfate, alluaudite-type  $\text{Na}_2\text{Fe}_2(\text{SO}_4)_3$ , is a star player.<sup>24</sup> It possesses of a high operating potential of 3.8 V vs  $\text{Na}^+/\text{Na}$ . Although the alluaudite  $\text{Na}_2\text{Fe}_2(\text{SO}_4)_3$  has very high operating potential, it is still lower than the highest value for Fe-based compounds in Li system.  $\text{LiFeSO}_4\text{F}$  has even higher potential of 3.9 V vs.  $\text{Li}^+/\text{Li}$ , which is highest Fe-redox potential for Li system.<sup>30-32</sup> Along with the favorable capacity, the extremely high theoretical energy density of  $\text{Na}_2\text{Fe}_2(\text{SO}_4)_3$  makes the sodium ion battery competitive with the state-of-art lithium ion battery. Therefore, it has captured great attention since first introduced by Barpanda *et al* in 2014.<sup>24</sup> Oyama *et al.* and ming *et al.* investigated the phase equilibrium of  $\text{Na}_{2+2x}\text{Fe}_{2-x}(\text{SO}_4)_3$  and demonstrated the stability of the off-stoichiometry in the system following up the initial report.<sup>25,26</sup> Wong *et al.* demonstrated the fairly fast sodium ion mobility in the framework of  $\text{Na}_2\text{Fe}_2(\text{SO}_4)_3$

by DFT simulations.<sup>27</sup> Wang *et al.* fabricated a full Na-ion cell based on the alluaudite  $\text{Na}_2\text{Fe}_2(\text{SO}_4)_3$  positive and  $\text{Ti}_2\text{C}$  negative electrode, which provides a promising framework for high performance Na-ion hybrid capacitors.<sup>28</sup> More recently, dwibedi *et al.* introduced a new Mn-homologue of  $\text{Na}_{2+2x}\text{Mn}_{2-x}(\text{SO}_4)_3$  in alluaudite family,<sup>29</sup> which has isostructure to  $\text{Na}_2\text{Fe}_2(\text{SO}_4)_3$  and attests to the richness of alluaudite sulfate chemistry.

Despite the flourishing development of alluaudite sulfate family, their synthetic strategy is very poor. Until now, all the alluaudite sulfates are prepared by the same approach as that in Barpanda's report, *i.e.* the low-temperature solid-state reaction.<sup>24</sup> It usually requires long time pretreatment, *e.g.* preparation of dehydrated  $\text{FeSO}_4$  for 12 hours and ball-mill of raw materials for 6 hours, to obtain uniform precursor before calcination.<sup>25-28</sup> The preparation process is time consuming and the morphology of product is random, which restricts both large-scale production and fast electron/ion transport for the alluaudite material. Therefore, a feasible synthetic method is needed to prepare alluaudite sulfate with increased efficiency and tailored particle morphology.

Nature has been a valuable and innovative source of inspiration for scientists due to the amazing properties of biological systems.<sup>33,34</sup> Especially, the fabulous texture and complex metabolizable action of the biological organisms such as animals or human being have offered us great inspiration.<sup>35,36</sup> Muscle tissue is a perfect example. As illustrated in Figure 1, the muscle is constructed by the myofibrils and closely wired blood vessels and nerves, which has high-efficiency nutrient supply and high-sensitive responsiveness during producing movement or generating heat. Therefore, it has two obvious advantages on both texture and function, *i.e.* the superior properties of fast mass exchange and the fabulous texture of high surface and superior strength. Both greatly inspire us to design new electrode materials for advanced batteries through mimicking its bio-structure.

Following this viewpoint, for the first time, we report a top-down approach to prepare alluaudite-type  $\text{Na}_{2+2x}\text{Fe}_{2-x}(\text{SO}_4)_3/\text{SWNT}$  spindles with muscle tissue-like architecture (Figure 2a). Firstly, the "top" material, *i.e.* the hydrated precursor, is prepared via a simple precipitation in short time (less than half

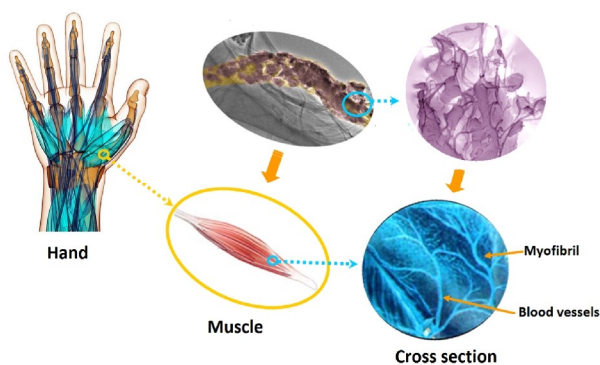


Figure 1. Scheme of muscle tissue-inspired  $\text{Na}_{2+2x}\text{Fe}_{2-x}(\text{SO}_4)_3/\text{SWNT}$  composite.

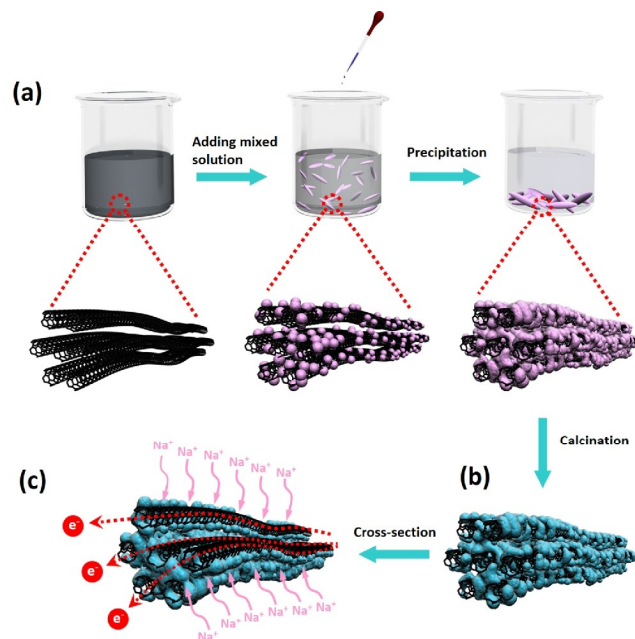


Figure 2 Scheme of the top-down synthetic approach and the structure of muscle-inspired  $\text{Na}_{2+2x}\text{Fe}_{2-x}(\text{SO}_4)_3/\text{SWNT}$  spindles. (a) Preparation process of the "top" hydrated precursor. (b) The structure of the "down" alluaudite product and (c) its cross-section image with fast electron and ion pathways. In a, the black ink is the carbon nanotube suspension; the solution in burette is the mixed solution of sodium sulfate ( $\text{Na}_2\text{SO}_4$ ) and hydrate iron sulfate ( $\text{FeSO}_4 \cdot 7\text{H}_2\text{O}$ ); the pink sphere is the hydrated precursor particles. In b, the blue sphere is the target alluaudite sulfate particle.

an hour). Then, the "down" material, *i.e.* the alluaudite-type product, is prepared by alleviated release of the hydration water from the precursor. The whole synthetic process is easy handling and timesaving, and moreover, the product has uniform composition and well-defined morphology. As illustrated in Figure 2b and c, the prepared alluaudite  $\text{Na}_{2+2x}\text{Fe}_{2-x}(\text{SO}_4)_3$  crystals are closely anchored on the single wall carbon nanotubes (SWNT), and aggregate into a spindle-shaped particle. The SWNT-based three-dimensional conductive framework facilitates the fast electron transport, and the voids between carbon nanotubes and crystals enable fast ion transport. Therefore, the  $\text{Na}_{2+2x}\text{Fe}_{2-x}(\text{SO}_4)_3/\text{SWNT}$  spindle copies both the architecture and function of the muscle tissue.

Inspired by these advantages, the sodium intercalation chemistry of  $\text{Na}_{2+2x}\text{Fe}_{2-x}(\text{SO}_4)_3/\text{SWNT}$  spindle was investigated in present study. The enhanced physicochemical properties, including improved electronic conductivity and ion diffusion capability, good high-rate capability and cycling stability, demonstrate the superiority of muscle tissue-inspired structure in energy storage systems.

## 2 Experimental

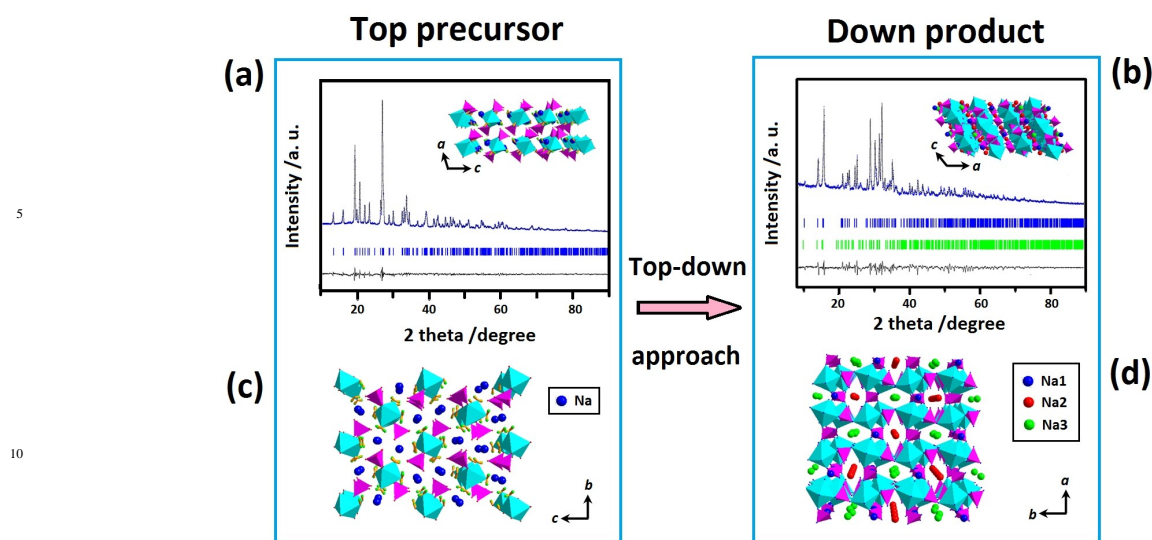


Figure 3 Rietveld refinement results of XRD data (a,b) and crystal structures (c,d) of the top precursor (a,c) and the down product (b,d). The blue ticks in *a* represent the Bragg peak positions of the  $\text{Na}_2\text{Fe}(\text{SO}_4)_2 \cdot 4\text{H}_2\text{O}$  phase in the top precursor (a). The blue and green ticks in *b* respectively represent the Bragg peak positions of the  $\text{Na}_{2+2x}\text{Fe}_{2-x}(\text{SO}_4)_3$  and  $\text{Na}_6\text{Fe}(\text{SO}_4)_4$  phases in the down product (b). The experimental data (blue crosses), calculated profile (black line) and their differences are indicated. Insets: projections of the structure of  $\text{Na}_2\text{Fe}(\text{SO}_4)_2 \cdot 4\text{H}_2\text{O}$  (a) and  $\text{Na}_{2+2x}\text{Fe}_{2-x}(\text{SO}_4)_3$  (b) along the *b*-axis. The cyan octahedron and magenta tetrahedral represent the  $\text{FeO}_6$  and  $\text{SO}_4$  units (c,d). The H atoms and O-H bond in top precursor (c) are indicated by small green balls and yellow ticks respectively.

### 2.1 “Top-down” Synthesis

**Synthesis of the “top” precursor** The “top” hydrated precursor is prepared by a low-temperature precipitation process (Figure 2a). Firstly, equal molar of sodium sulfate ( $\text{Na}_2\text{SO}_4$ ) and hydrate iron sulfate ( $\text{FeSO}_4 \cdot 7\text{H}_2\text{O}$ ) with a desirable amount of iron wires were dissolved in 8 ml distilled water to form a uniform mixture (A). Single-wall carbon nanotube (Najing XFNANO Materials Tech Co., Ltd.) was dispersed in 40 ml ethanol under ultrasonication for six hours to build a uniform suspension (B). After removal of the iron wires from the mixture (A), it was added to the suspension (B) dropwise under strong stirring. After sufficient precipitation (~half an hour), the product was filtered and washed with ethanol. Finally, the product was dried in a vacuum oven at  $50^\circ\text{C}$  to achieve the precursor.

**Synthesis of the “down” product** The “down” product is prepared by a calcination process. The obtained top precursor is annealed at  $200^\circ\text{C}$  for 2 hours and  $350^\circ\text{C}$  for 6 hours at the heating rate of  $1^\circ\text{C}\cdot\text{min}^{-1}$  in Ar atmosphere and then quenched to room temperature to achieve the final “down” product.

**Synthesis of the reference sample** For comparison, the pristine samples were prepared in the same approach, only without SWNT during the synthetic process of “top” precursor.

### 2.2 Characterization

Powder X-ray diffraction (XRD, Bruker D8/Germany) using  $\text{Cu K}\alpha$  radiation was employed to identify the crystalline phase of the material. The experiment was performed by using step mode with

a fixed time of 3 s and a step size of  $0.02^\circ$ . The XRD pattern was refined by using the Rietveld method. The morphology was observed with a scanning electron microscope (SEM, HITACHI-4700) and a transmission electron microscope (TEM, JEOS-2010 PHILIPS). Inductively coupled plasma atomic emission spectroscopy (ICP) is employed to investigate the elemental composition of prepared material. Nitrogen adsorption-desorption isotherms were measured using a Micro-meritics ASAP 2010 sorptometer and specific surface and pore size distribution were calculated correspondingly. Carbon contents of the samples were determined by an element analyzer (EA, Elementar Vario EL). The electronic conductivity was measured on the pellet of powder. The powder was pressed into a disk with gold painted on both sides to ensure electrical contact.

### 2.3 Electrochemical measurements

The electrochemical characteristics were measured in CR2032 coin cells. The coin cells were assembled in an argon filled glove box. Each composite electrode was made from a mixture of the active material, carbon black and polyvinylidene fluoride (PVDF) in a weight ratio of 8:1:1. Na foil was employed as counter and reference electrode and  $1\text{ mol}\cdot\text{L}^{-1}$   $\text{NaClO}_4$  dissolved in propylene carbonate (PC) was used as electrolyte. Galvanostatic charge-discharge tests were performed in the potential range of 2.0~4.5 V vs.  $\text{Na}^+/\text{Na}$  at ambient temperature on a Land battery testing system (Wuhan, China). EIS measurements were conducted at a fully discharged state using a Zivelab electrochemical workstation, and the applied frequency range is  $100\text{k}\sim 0.5\text{ mHz}$ .

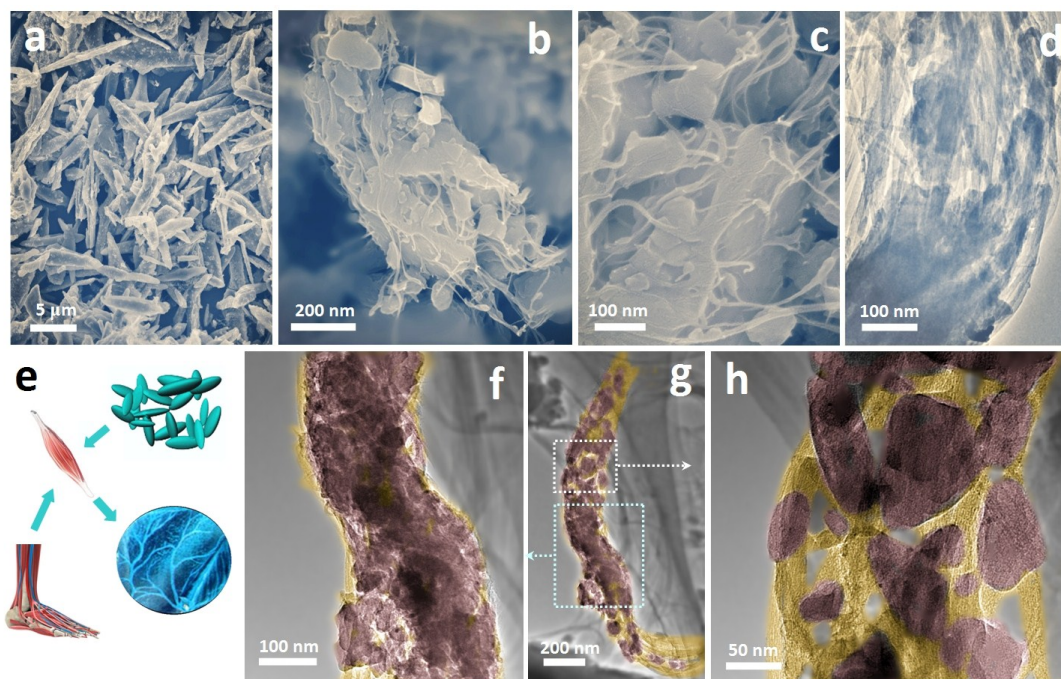
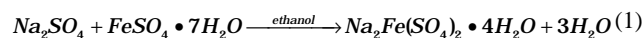


Figure 4 Morphology of the muscle-inspired  $\text{Na}_{2+2x}\text{Fe}_{2-x}(\text{SO}_4)_3/\text{SWNT}$  spindles. SEM and TEM images of the composite in low (a) and high magnifications (b,c,d). (g) TEM images of a single spindle with enlarged images in white and blue rectangles (f, h). (e) The schematic images of a single piece of muscle and its internal structure with blood vessels and nerves.

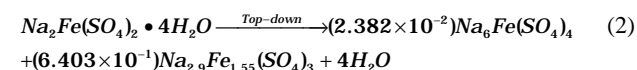
### 3 Results and Discussion

#### 3.1 Structure evolution during top-down approach

The phase transformation process during the top-down approach is investigated by XRD results. Figure 3a and b exhibits the Rietveld results of both the top precursor and the down product. The detailed structural parameters of both materials are listed in Table S1 and S2. There is only one hydrated sulfate phase, *i.e.*  $\text{Na}_2\text{Fe}(\text{SO}_4)_2 \cdot 4\text{H}_2\text{O}$ , in the top precursor, demonstrating the successful synthesis of the single-phase precursor. The reaction for preparation of the top precursor can be displayed as following equation (1),



After dehydration in the calcination process, the down product is achieved. As displayed in Figure 3b, there are two phases, *i.e.* the target  $\text{Na}_{2+2x}\text{Fe}_{2-x}(\text{SO}_4)_3$  and  $\text{Na}_6\text{Fe}(\text{SO}_4)_4$  impurity, coexist in the product. Based on the Rietveld refinement results, the ratio of  $\text{Na}_{2+2x}\text{Fe}_{2-x}(\text{SO}_4)_3$  and  $\text{Na}_6\text{Fe}(\text{SO}_4)_4$  is 95.38 wt.% : 4.62 wt.%. Therefore, the exact composition of  $\text{Na}_{2+2x}\text{Fe}_{2-x}(\text{SO}_4)_3$  can be deduced to be  $\text{Na}_{2.9}\text{Fe}_{1.55}(\text{SO}_4)_3$  ( $x=0.45$ ), and the phase transformation process during the top-down approach can be displayed as following equation (2),



The results demonstrate that the off-stoichiometric alluaudite-type sulfate can be achieved by present strategy. It is coincided with the phase-equilibrium theory of  $\text{Na}_2\text{SO}_4\text{-FeSO}_4$

introduced by oyama,<sup>25</sup> which has demonstrated the stability of off-stoichiometry alluaudite  $\text{Na}_{2+2x}\text{Fe}_{2-x}(\text{SO}_4)_3$ . Moreover, it is also provides an indirect clue for the metastable nature of  $\text{Na}_2\text{Fe}(\text{SO}_4)_2$  phase, which was first introduced by Reynaud<sup>19</sup> *et al* through slowly dehydration of  $\text{Na}_2\text{Fe}(\text{SO}_4)_2 \cdot 4\text{H}_2\text{O}$  at 120~260 °C, and then discussed as metastable phase by oyama *et al.*<sup>25</sup> The off-stoichiometry in the alluaudite material is further confirmed by ICP analysis, which determined the Na/Fe element ratio to be 1.874 that is close to the refined derived value of 1.871. Therefore, all of the advantages of present top-down approach, including the easy handling, friendly condition and timesaving, make it a favorable strategy for large-scale production of the alluaudite sulfates.

The crystal structures of the top precursor and the down product are illustrated in Figure 3c and d. It doesn't seem to have obvious structural relationship between these materials. On the one hand, the hydrate sulfate precursor adopts the bloedite structure (Figure 3c). It is built by the isolated  $\text{Fe}(\text{SO}_4)_2(\text{H}_2\text{O})_4$  units, which are constructed by one  $\text{FeO}_2(\text{OH})_4$  octahedron and two  $\text{SO}_4$  tetrahedra. Sodium ions locate at large channels and are coordinated by six oxygen atoms. On the other hand, the down product adopts an alluaudite-type framework (Figure 3d). The adjacent distorted  $\text{FeO}_6$  octahedra share an equatorial edge to form isolated  $\text{Fe}_2\text{O}_{10}$  groups, which are in turn linked by  $\text{SO}_4$  tetrahedra. They form a three-dimensional structure with large cavities along the *c*-axis, and three different types of sodium ions located at two kinds of cavities. The big structural difference between the top and down materials demonstrates the entirely phase transformation accompanying dehydration under present synthetic condition. It provides a new structure evolution

mechanism of top-down strategy for the sulfates family. Therefore, it is a new route for the fast and easy preparation of the alluaudite-type sulfates on large scale.

### 3.2 Muscle-inspired $\text{Na}_{2+2x}\text{Fe}_{2-x}(\text{SO}_4)_3/\text{SWNT}$ spindle

The morphology of prepared  $\text{Na}_{2+2x}\text{Fe}_{2-x}(\text{SO}_4)_3/\text{SWNT}$  composite is characterized by SEM and TEM observations. Based on the low-magnification SEM observation (Figure 4a), the composite has uniform spindle-shaped particles. The ratio of the length to the diameter of cross-section for the spindles are in the range of 10~20. The enlarged SEM (Figure 4b, c) and TEM images (Figure 4d, f, g) demonstrate the  $\text{Na}_{2+2x}\text{Fe}_{2-x}(\text{SO}_4)_3$  nanoparticles with the size of 50~100 nm are well encompassed by single wall carbon nanotubes. They form a three-dimensional conductive framework and enable fast electron transport. More detailed analysis is identified by HRTEM images (Figure 4h). It indicates the existence of voids between the carbon nanotubes and the sulfates, which results in the micro/macro-pores inside the spindle particles. It not only facilitates good contact between the electrolyte and the sulfate active material, but also promotes high-efficiency ion transport.

Therefore, the  $\text{Na}_{2+2x}\text{Fe}_{2-x}(\text{SO}_4)_3/\text{SWNT}$  composite copy the muscle tissue on both morphology and the function (Figure 4e). Firstly, its spindle shape morphology and the internal SWNT-based structure are similar to the architecture of muscle tissue, which have plenty of blood vessels and nerves closely wiring the myofibrils. Moreover, its facile electron/ion pathways ensure fast sodium intercalation chemistry, which is functionally similar to the high-efficiency nutrient supply, fast mass transport and robust metabolism of the muscle.

Nitrogen sorption isotherms are generated to investigate the Brunauer-Emmett-Teller (BET) surface and the porosity of the  $\text{Na}_{2+2x}\text{Fe}_{2-x}(\text{SO}_4)_3/\text{SWNT}$  spindles. As displayed in Figure 5, the significant hysteresis loop confirms the porous structure of the composite, which possesses a high specific surface area of  $64.1 \text{ m}^2 \cdot \text{g}^{-1}$  and a large pore volume of  $0.16 \text{ cm}^3 \cdot \text{g}^{-1}$ . The results confirm the porous structure of prepared composite, which are coincided with above SEM and TEM observation results.

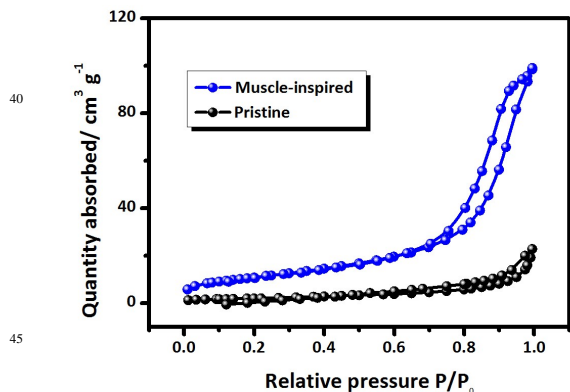


Figure 5  $\text{N}_2$  sorption isotherms of the muscle-inspired  $\text{Na}_{2+2x}\text{Fe}_{2-x}(\text{SO}_4)_3/\text{SWNT}$  composite and the carbon-free reference sample.

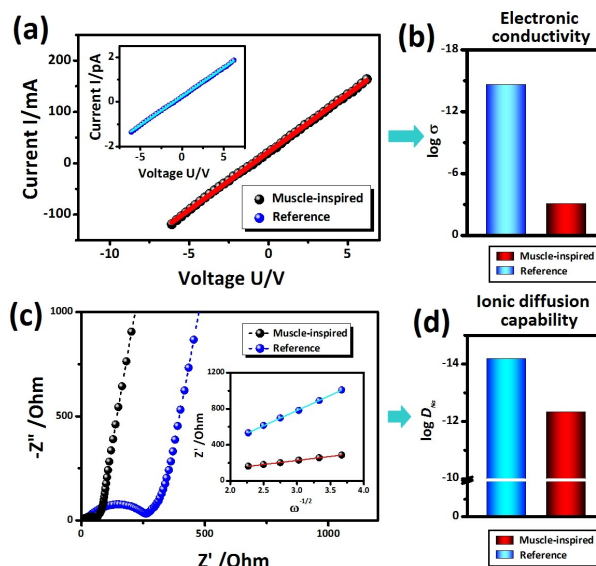


Figure 6 (a) Current-voltage response of the muscle-inspired  $\text{Na}_{2+2x}\text{Fe}_{2-x}(\text{SO}_4)_3/\text{SWNT}$  composite and the carbon-free reference sample (inset). (b) Comparison of the calculated electronic conductivities between both samples. (c) Nyquist plots and linear relationship of the  $Z''$  and the reciprocal square root of frequency in the low frequency region (inset). (d) Comparison of calculated sodium diffusion coefficients between both samples.

Moreover, a reference sample of the carbon-free  $\text{Na}_{2+2x}\text{Fe}_{2-x}(\text{SO}_4)_3$  is employed to clarify the advantages of the muscle-inspired architecture. It is prepared in the same approach as the muscle-inspired sample only without the employment of SWNTs. The detailed physical characteristics of both samples are compared in Table S3. The reference sample exhibits the BET surface and pore volume of  $6.2 \text{ m}^2 \cdot \text{g}^{-1}$  and  $0.03 \text{ cm}^3 \cdot \text{g}^{-1}$  respectively. The low porosity and BET surface area is associated with its large, solid and carbon free particles (Figure s1, table S3). Therefore, the above results demonstrate the superiority in the electrolyte/electrode interface and porosity for the muscle-inspired architecture, which facilitate electrolyte penetration and fast ion transport.

### 3.3 Electronic and ion conductivity

The electronic and ion transport capability of the  $\text{Na}_{2+2x}\text{Fe}_{2-x}(\text{SO}_4)_3/\text{SWNT}$  composite and pristine sample are estimated at room temperature. As displayed in Figure 6(a), the electronic conductivity ( $\sigma$ ) is calculated based on the linear fits of the current-voltage curves. It is about  $2.3 \times 10^{-15} \text{ s} \cdot \text{cm}^{-1}$  for the pristine  $\text{Na}_{2+2x}\text{Fe}_{2-x}(\text{SO}_4)_3$  at ambient temperature (Figure 6b), which is in agreement with the previously reported sulfates such as  $\text{Li}_2\text{Fe}(\text{SO}_4)_2$  ( $\sigma \sim 10^{-16} \text{ s} \cdot \text{cm}^{-1}$ ),<sup>37</sup>  $\text{Li}_2\text{Co}(\text{SO}_4)_2$  (monoclinic phase,  $\sigma \sim 10^{-18} \text{ s} \cdot \text{cm}^{-1}$ ; orthorhombic phase,  $\sigma \sim 10^{-14} \text{ s} \cdot \text{cm}^{-1}$ )<sup>38</sup> and  $\text{Na}_2\text{Fe}(\text{SO}_4)_2 \cdot 2\text{H}_2\text{O}$  ( $\sigma \sim 10^{-15} \text{ s} \cdot \text{cm}^{-1}$ ).<sup>21</sup> All these electronic conductivity values of the sulfates were much lower than the other polyanion materials, such as the most commonly  $\text{LiFePO}_4$  ( $\sigma \sim 10^{-9} \text{ s} \cdot \text{cm}^{-1}$ ).<sup>39</sup> Thus the poor conductivity is a serious problem for sulfates-based electrode materials. Significant improvement

was observed for the hierarchical composite, which increased to about  $8.3 \times 10^{-4} \text{ s} \cdot \text{cm}^{-1}$  at room temperature. The enhanced conductivity is associated with the unique architecture of the muscle-inspired composite, which has SWNT-based 3D conductive network and ensures fast electron transport.

Electrochemical impedance spectroscopy (EIS) techniques are employed to evaluate the ion diffusion capability. As displayed in Figure 6 (c). Each Nyquist plot consists of a depressed semicircle and a sloping line. The depressed semicircle and the sloping line can be attributed to the charge transfer process and the solid-state diffusion of sodium ion, respectively.<sup>40,41</sup> The depressed semicircle of the muscle-inspired sample is much lower than that of the pristine one, demonstrating its lower charge transfer resistance ( $R_{ct}$ ). The sodium diffusion capability can be evaluated by the low frequency sloping line (Supporting information S1). Based on the linear relationship of the  $Z'$  and the reciprocal square root of frequency in the low frequency region (inset of Figure 6c), the sodium diffusion coefficients of both samples ( $D_{Na}$ ) are calculated. The muscle-inspired composite exhibits the  $D_{Na}$  value of  $4.67 \times 10^{-13} \text{ cm}^2 \text{ s}^{-1}$ , which is about two orders higher than the pristine one ( $6.45 \times 10^{-15} \text{ cm}^2 \text{ s}^{-1}$ ). Therefore, both the lower charge transfer resistance and higher sodium diffusion coefficient demonstrate the enhanced sodium transfer capability of the muscle-inspired sample.

The superior electron/ion conductivity of the  $\text{Na}_{2+2x}\text{Fe}_{2-x}(\text{SO}_4)_3/\text{SWNT}$  composite can be attributed to its unique architecture. As discussed above, the muscle-inspired structure not only ensures high-efficient ion transport by porous architecture, but also provides continuous electron transport pathways through constructing 3D conductive network. Both facilitate the sodium intercalation and do good to the electrochemical property. Thus, the results confirm that the muscle-inspired architecture is highly efficient in modifying the ion intercalation kinetics for the alluaudite sulfates.

### 3.4 Sodium intercalation chemistry

Inspired by the advantages of muscle-inspired architecture, the sodium intercalation chemistry of the  $\text{Na}_{2+2x}\text{Fe}_{2-x}(\text{SO}_4)_3/\text{SWNT}$  composite is investigated. First of all, the reaction mechanism of the sodium intercalation is investigated. Figure 7 displays the galvanostatic charge/discharge curves and the corresponding *ex-situ* XRD patterns measured at different potentials. Both charge/discharge processes feature the sloping curves without obvious potential plateau, indicating a single-phase reaction mechanism. The diffraction peaks of *ex-situ* XRD patterns continuously slightly shift to high-angle during charging and change reversely during discharging. No extra new peak is formed in the entire charge/discharge process. All the results demonstrate the single-phase homogenous reaction for the alluaudite  $\text{Na}_{2+2x}\text{Fe}_{2-x}(\text{SO}_4)_3$  during sodium intercalation, which agrees well with previous reports.<sup>24</sup> The single-phase reaction mechanism avoids large volume change during the sodium de/intercalation process, which is beneficial to the electrochemical performance of the alluaudite sulfate electrode.

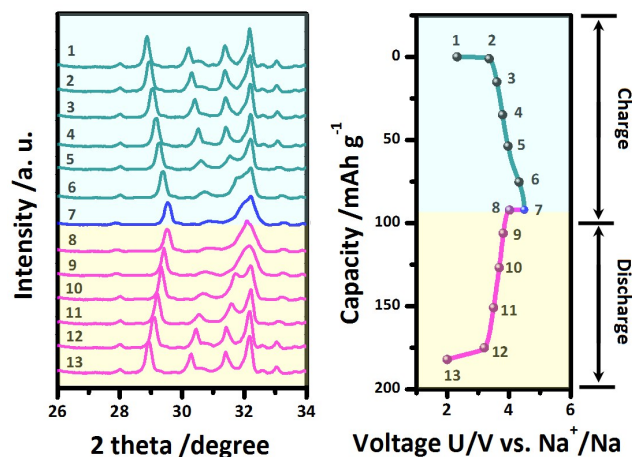


Figure 7 Galvanostatic charge/discharge curves of the  $\text{Na}_{2+2x}\text{Fe}_{2-x}(\text{SO}_4)_3/\text{SWNT}$  composite (right) and the corresponding *ex-situ* XRD patterns (left) measured at different potentials

Next, the galvanostatic charge/discharge measurements were carried out on the muscle-inspired  $\text{Na}_{2+2x}\text{Fe}_{2-x}(\text{SO}_4)_3/\text{SWNT}$  composite and the carbon-free reference sample. Figure 8(a) displays the charge/discharge curves of the  $\text{Na}_{2+2x}\text{Fe}_{2-x}(\text{SO}_4)_3/\text{SWNT}$  composite in the initial three cycles. An obvious higher potential was observed in the initial charge curve, which drops in the subsequent cycles. Similar phenomenon has also been observed in stoichiometric  $\text{Na}_2\text{Fe}_2(\text{SO}_4)_3$  and other materials such as  $\text{Li}_2\text{FeSiO}_4$  and  $\text{Li}_2\text{FeP}_2\text{O}_7$ .<sup>24,42-46</sup> It may be associated with the occurrence of some irreversible structural transformation during first desodiation process, as indicated in previous report.<sup>24</sup> After the initial cycle, the high potential of  $\sim 3.78 \text{ V}$  (vs.  $\text{Na}^+/\text{Na}$ ) is observed for the muscle-inspired sample, which demonstrates its high operating potential. Figure 8 (b) and (c) display the rate capability of both muscle-inspired and the pristine samples. A series of current densities, including  $0.05 C$ ,  $0.2 C$ ,  $0.5 C$ ,  $1 C$ ,  $2 C$ ,  $5 C$ ,  $10 C$ ,  $20 C$  and  $40 C$ , are employed. Both samples exhibit similar capacities as the current density is lower than  $0.5 C$ . When the current density increases to  $1 C$ , obvious higher capacities are observed for the muscle-inspired sample than the pristine one. The differences between two samples become more significant as the current density further increases. For example, the muscle-inspired composite delivers  $85.3$  and  $74.9 \text{ mAh} \cdot \text{g}^{-1}$  of the capacities at the  $1 C$  and  $10 C$  rates, but only  $80.1$  (at  $1 C$ ) and  $52.3 \text{ mAh} \cdot \text{g}^{-1}$  (at  $10 C$ ) of capacities are obtained for the pristine material. The superb rate capability of the  $\text{Na}_{2+2x}\text{Fe}_{2-x}(\text{SO}_4)_3/\text{SWNT}$  composite can be attributed to its well-defined architecture as illustrated in Figure 2. 3D conductive framework as well as efficient sodium-ion diffusion enables rapid sodium-ion extraction/insertion and results in good high rate capability.

Finally, the cycling performances of both samples are investigated. As displayed in Figure 8(d) and (e), the capacity retentions of  $97\%$  and  $92\%$  are obtained for the muscle-inspired sample at  $0.5 C$  and  $5 C$ , which is higher than those of the pristine one ( $76\%$  at  $0.5 C$  and  $64\%$  at  $5 C$ ). After the cycling test, both

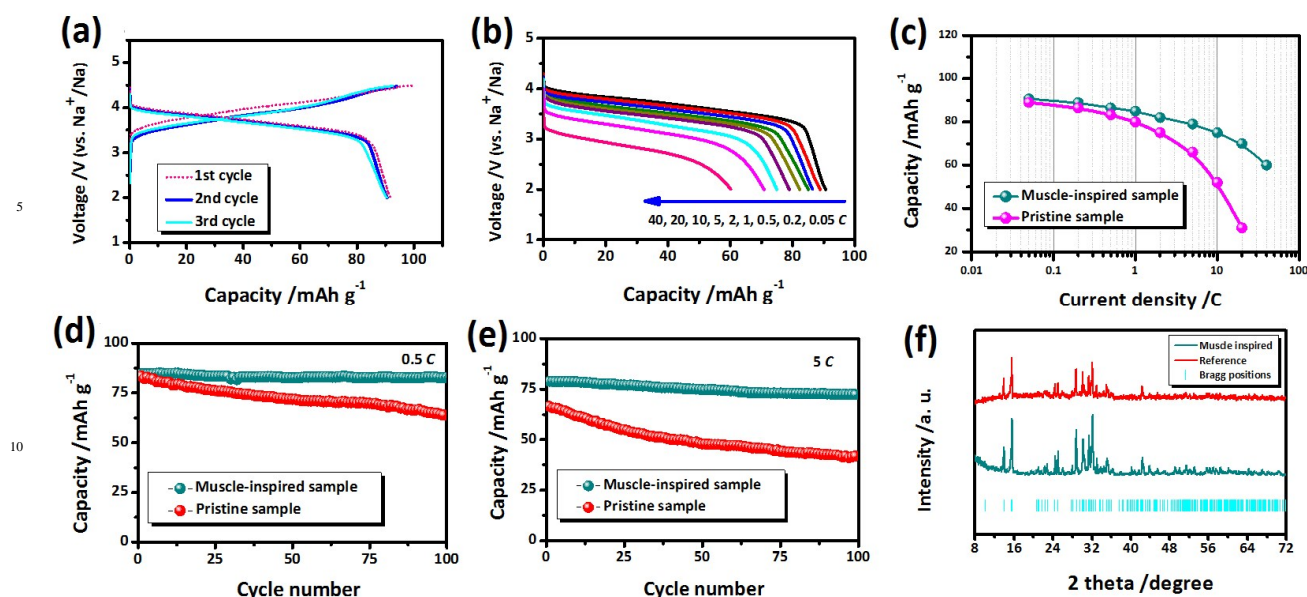


Figure 8 (a) Galvanostatic charge/discharge curves of the muscle-inspired  $\text{Na}_{2+2x}\text{Fe}_{2-x}(\text{SO}_4)_3/\text{SWNT}$  spindle in the initial three cycles at 0.05 C. (b) Discharge curves of the muscle-inspired  $\text{Na}_{2+2x}\text{Fe}_{2-x}(\text{SO}_4)_3/\text{SWNT}$  spindle at different rates from 0.05 to 40 C. (c) Comparison of the rate capability between the muscle-inspired spindle and pristine sample. (d,e) Long-term cycling performance of the muscle-inspired spindle and pristine sample at 0.5 C (d) and 5 C (e). (f) XRD patterns of the muscle-inspired spindle and pristine sample after cycles.

materials were recovered and subjected to XRD measurement. Both cycled materials exhibit similar patterns and coincide with the standard alluaudite structure (Figure 8f), indicating their small structure changes during repeated sodium de/intercalation. It coincides with the single-phase homogenous reaction mechanism of alluaudite sulfate as discussed above. Compared with the pristine sample, higher peak intensities are observed for the muscle-inspired one, indicating its better structure stability during cycling. It is associated with the SWNT-based framework and porous structure in the muscle-inspired architecture. They guarantee the effective electron contact and act as the buffer layer to alleviate volume change during sodium insertion/extraction. Therefore, all above results demonstrate the muscle-inspired architecture is favorable to realizing high rate capability and stable cycling property for the alluaudite sulfate, which puts forwards a new strategy to modify the sulfate-based materials in sodium ion batteries.

## 4 Conclusions

In summary, we have reported a new “top-down” approach to prepare muscle-inspired  $\text{Na}_{2+2x}\text{Fe}_{2-x}(\text{SO}_4)_3/\text{SWNT}$  spindle. The hydrated “top” precursor is prepared by rapid precipitation, which undergoes hydration water release and phase transformation during the following calcination to achieve the target “down” product. The prepared alluaudite sulfate nanoparticles are anchored on the single-wall carbon nanotubes and aggregate into spindle-shaped particles. The whole  $\text{Na}_{2+2x}\text{Fe}_{2-x}(\text{SO}_4)_3/\text{SWNT}$  composite copies the muscle tissue on both morphology and function. Based on the SWNT-based 3D conductive framework and the porous structure, the muscle-inspired architecture

enables high efficiency electron/ion transport and superior sodium intercalation kinetics. It exhibit high potential of  $\sim 3.8$  V (vs.  $\text{Na}^+/\text{Na}$ ) and superior high rate performance, which achieves 92% of the capacity after one hundred cycles at 5 C. Therefore, the top-down approach is facile strategy to prepare alluaudite sulfate with tailored architecture.

## Acknowledgement

This work is supported by the Natural Science Funds for Distinguished Young Scholar of Heilongjiang Province (No. JC2015001), Program for New Century Excellent Talents in Heilongjiang Provincial University (No. 1253-NCET-012) and Natural Science Foundation of Heilongjiang Province (No. QC2013C008).

## Notes and references

<sup>a</sup>Key Laboratory for Photonic and Electronic Bandgap Materials, Ministry of Education; College of Chemistry and Chemical Engineering, Harbin Normal University, Harbin, 150025, Heilongjiang, China; E-Mail: chaodenghsd@sina.com

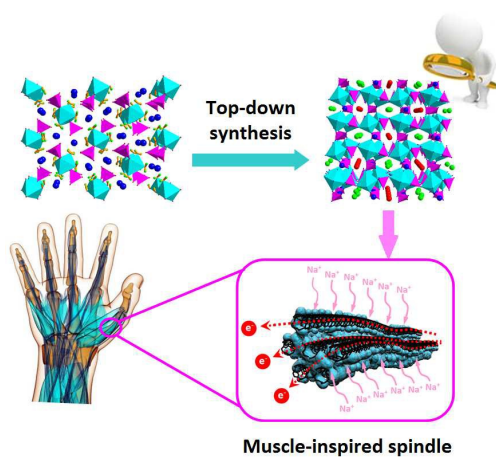
<sup>b</sup>Key Laboratory of Superlight Material and Surface Technology, Ministry of Education, College of Material Science and Chemical Engineering, Harbin Engineering University, Harbin 150001, Heilongjiang, China; E-Mail: senzhang@hrbeu.edu.cn

†Electronic Supplementary Information (ESI) available: Atomic parameters and lattice parameters of the precursor and product; SEM image of pristine sample and calculation of sodium intercalation coefficients. See DOI: 10.1039/b000000x/

1 D. Kundu, E. Talaie, V. Duffort, L. F. Nazar, *Angew. Chem. Int. Ed.* **2015**, *54*, 3431-3448.

- 2 L. P. Wang, L. H. Yu, X. Wang, M. Srinivasan, Z. J. Xu, *J. Mater. Chem. A* **2015**, *3*, 9353-9378.
- 3 J. A. Saint, M. M. Doeff, J. Wilcox, *Chem. Mater.* **2008**, *20*, 3404-3411.
- 5 4 R. Berthelot, D. Carlier, C. Delmas, *Nat. Mater.* **2011**, *10*, 74-80.
- 5 M. Sathiya, K. Hemalatha, K. Ramesha, J. Tarascon, A. Prakash, *Chem. Mater.* **2012**, *24*, 1846-1853.
- 6 M. Blesa, E. Moran, C. Leon, J. Santamaria, J. Tornero, N. Menendez, *Solid State Ion.* **1999**, *126*, 81-87.
- 10 7 C. Deng, S. Zhang, Z. Dong, Y. Shang, *Nano Energy* **2014**, *4*, 49-55.
- 8 H. Kim, R. A. Shakoor, C. Park, S. Y. Lim, J. S. Kim, Y. N. Jo, W. Cho, M. Miyasaka, Y. Jung, J. W. Choi, *Adv. Funct. Mater.* **2013**, *23*, 1147-1155.
- 15 9 B. D. Zhao, Q. Y. Wang, S. Zhang, C. Deng, *J. Mater. Chem. A* **2015**, *3*, 12089-12096.
- 10 K. H. Ha, S. H. Woo, D. G. Mok, N. S. Choi, Y. Park, S. M. Oh, Y. Kim, J. Kim, J. Lee, L. F. Nazar, K. T. Lee, *Adv. Energ. Mater.* **2013**, *3*, 770-776.
- 20 11 Q. Y. Wang, B. D. Zhao, S. Zhang, X. H. Gao, C. Deng, *J. Mater. Chem. A* **2015**, *3*, 7732-7740.
- 12 J. Song, M. W. Xu, L. Wang, J. B. Goodenough, *Chem. Commun.* **2013**, *49*, 5280-5282.
- 13 S. Y. Lim, H. Kim, J. Chung, J. H. Lee, B. G. Kim, J. J. Choi, K. Y. Chung, W. Cho, S. J. Kim, W. A. Goddard, Y. S. Jung, J. W. Choi, *PNAS* **2014**, *111*, 599-604.
- 25 14 C. Deng, S. Zhang, *ACS Appl. Mater. Interfaces* **2014**, *6*, 9111-9117.
- 15 S. Zhang, C. Deng, Y. Meng, *J. Mater. Chem. A* **2014**, *2*, 20538-20544.
- 30 16 C. Deng, S. Zhang, Y. X. Wu, *Nanoscale* **2015**, *7*, 487-491.
- 17 H. Kim, I. Park, D. H. Seo, S. Lee, S. W. Kim, W. J. Kwon, Y. U. Park, C. S. Kim, S. Jeon, K. Kang, *J. Am. Chem. Soc.* **2012**, *134*, 10369-10372.
- 35 18 H. L. Chen, G. Hautier, G. Ceder, *J. Am. Chem. Soc.* **2012**, *134*, 19619-19627.
- 19 M. Reynaud, G. Rousse, A. M. Abakumov; M. T. Sougrati, G. V. Tendeloo, J. N. Chotard, J. M. Tarascon, *J. Mater. Chem. A* **2014**, *2*, 2671-2680.
- 40 20 P. Barpanda, G. Oyama, C. D. Ling, A. Yamada, *Chem. Mater.* **2014**, *26*, 1297-1299.
- 21 Y. Meng, S. Zhang, C. Deng, *J. Mater. Chem. A* **2015**, *3*, 4484-4492.
- 22 M. Reynaud, P. Barpanda, G. Rouse, J. Chotard, B. Melot, N. Recham, J. M. Tarascon, *Solid State Sci.*, **2012**, *14*, 15-20.
- 45 23 P. Barpanda, J. N. Chotard, N. Recham, C. Delacourt, M. Ati, L. Dupont, M. Armand, J. M. Tarascon, *Inorg. Chem.* **2010**, *49*, 7401-7413.
- 24 P. Barpanda, G. Oyama, S. I. Nishimura, S. C. Chung, A. Yamada, *Nat. Commu.* **2014**, *5*, 4358.
- 50 25 G. Oyama, S. Nishimura, Y. Suzuki, M. Okubo, A. Yamada, *ChemElectroChem* **2015**, *2*, 1019-1023.
- 26 J. Ming, P. Barpanda, S. Nishimura, M. Okubo, A. Yamada, *Electrochem. Commun.* **2015**, *51*, 19-22.
- 55 27 L. L. Wong, H. M. Chen, S. Adams, *Phys. Chem. Chem. Phys.* **2015**, *17*, 9186-9193.
- 28 X. F. Wang, S. Kajiyama, H. Linuma, E. Hosono, S. Oro, I. Moriguchi, M. Okubo, A. Yamada, *Nat. Commu.* **2015**, *6*, 6544.
- 29 D. Dwibedi, R. B. Araujo, S. Chakraborty, P. P. Shanbogh, N. G. Sundaram, R. Ahuja, P. Barpanda, *J. Mater. Chem. A* **2015**, *3*, 18564-18571.
- 60 30 P. Barpanda, M. Ati, B. C. Melot, G. Rousse, J. N. Chotard, M. L. Doublet, M. T. Sougrati, S. A. Corr, J. C. Jumas, J. M. Tarascon, *Nat. Mater.*, **2011**, *10*, 772-779.
- 65 31 M. Ati, B. C. Melot, G. Rousse, J. N. Chotard, P. Barpanda, J. M. Tarascon, *Angew. Chem. Int. Ed.*, **2011**, *50*, 10574-10577.
- 32 P. Barpanda, *Isr. J. Chem.*, **2015**, *55*, 537-557.
- 33 L. Zhang, J. Wu, Y. Wang, Y. Long, N. Zhao, J. Xu, *J. Am. Chem. Soc.* **2012**, *134*, 9879-9881.
- 70 34 S. Wang, S. Chen, Q. Wei, X. Zhang, S. Wong, S. Sun, X. Li, *Chem. Mater.* **2015**, *27*, 336-342.
- 35 B. D. Zhao, B. Lin, S. Zhang, C. Deng, *Nanoscale* **2015**, DOI:10.1039/C5NR06505D
- 36 D. Y. Chung, K. J. Lee, S. H. Yu, M. Kim, S. Y. Lee, O. H. Kim, H. J. Park, Y. E. Sung, *Adv. Energy Mater.* **2015**, *5*, 1401309-1401317.
- 75 37 L. Lander, M. Reynaud, G. Rousse, M. T. Sougrati, C. L. Robert, R. J. Messinger, M. Deschamps, J. M. Tarascon, *Chem. Mater.* **2014**, *26*, 4178-4189.
- 38 J. M. Lark, C. Eames, M. Reynaud, G. Rousse, J. N. Chotard, J. M. Tarascon, M. S. Islam, *J. Mater. Chem. A* **2014**, *2*, 7446-7453.
- 80 39 P. S. Herle, B. Ellis, N. Coombs, L. F. Nazar, *Nat. Mater.* **2004**, *3*, 147-152.
- 40 S. Zhang, C. Deng, H. Gao, F. L. Meng, M. Zhang, *Electrochim. Acta* **2013**, *107*, 406-412.
- 85 41 J. Bard, L. R. Faulkner, *Electrochemical methods*, 2nd ed., Wiley, New York, 2001.
- 42 C. Deng, S. Zhang, S. Y. Yang, B. L. Fu, L. Ma, *J. Power Sources*, **2011**, *196*, 386-392.
- 43 C. Deng, S. Zhang, S. Y. Yang, *Mater. Chem. Phys.* **2010**, *120*, 14-17.
- 90 44 S. Nishimura, M. Nakamura, R. Natsui, A. Yamada, *J. Am. Chem. Soc.* **2010**, *132*, 13596-13597.
- 45 P. Barpanda, T. Ye, S. C. Chung, Y. Yamada, S. I. Nishimura, A. Yamada, *J. Mater. Chem.* **2012**, *22*, 13455-13459.
- 95 46 L. Tan, S. Zhang, C. Deng, *J. Power Sources*, **2015**, *275*, 6-13.

## Graphic Abstract



A top-down strategy is designed as a facile approach to prepare the alluaudite  $\text{Na}_{2+2x}\text{Fe}_{2-x}(\text{SO}_4)_3$  with muscle-like shape and superior performance.